

pubs.acs.org/est Article

Elucidating the Role of Single-Atom Pd for Electrocatalytic Hydrodechlorination

Dahong Huang,[#] David J. Kim,[#] Kali Rigby, Xuechen Zhou, Xuanhao Wu, Aidan Meese, Junfeng Niu,* Eli Stavitski, and Jae-Hong Kim*



Cite This: Environ. Sci. Technol. 2021, 55, 13306-13316



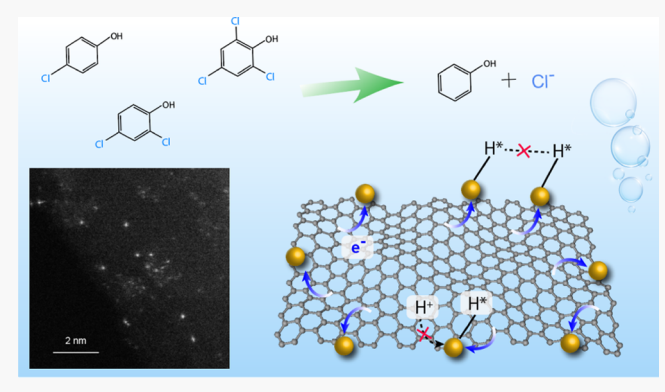
ACCESS

Metrics & More

Article Recommendations

SI Supporting Information

ABSTRACT: In this study, we loaded Pd catalysts onto a reduced graphene oxide (rGO) support in an atomically dispersed fashion [i.e., Pd single-atom catalysts (SACs) on rGO or Pd₁/rGO] via a facile and scalable synthesis based on anchor-site and photo-reduction techniques. The as-synthesized Pd₁/rGO significantly outperformed the Pd nanoparticle (Pd_{nano}) counterparts in the electrocatalytic hydrodechlorination of chlorinated phenols. Downsizing Pd_{nano} to Pd₁ leads to a substantially higher Pd atomic efficiency (14 times that of Pd_{nano}), remarkably reducing the cost for practical applications. The unique single-atom architecture of Pd₁ additionally affects the desorption energy of the intermediate, suppressing the catalyst poisoning by Cl⁻, which is a prevalent challenge with Pd_{nano}. Characterization and experimental results demonstrate that the superior performance of Pd₁/rGO originates



from (1) enhanced interfacial electron transfer through Pd–O bonds due to the electronic metal–support interaction and (2) increased atomic H (H*) utilization efficiency by inhibiting H_2 evolution on Pd_1 . This work presents an important example of how the unique geometric and electronic structure of SACs can tune their catalytic performance toward beneficial use in environmental remediation applications.

KEYWORDS: single-atom catalyst, palladium, reduced graphene oxide, hydrogenation, cathodic dechlorination, electronic metal—support interaction (EMSI)

■ INTRODUCTION

Chlorinated phenols and phenolic compounds (CPs) represent a broad variety of pollutants that are widely detected in the environment as harmful disinfection byproducts during chlorination-based treatments and from their extensive applications as components of pharmaceuticals, biocides, pesticides, and herbicides.^{2–4} The presence of chlorine atoms leads to the acute toxicity, genetic toxicity, and carcinogenicity,⁵⁻⁷ posing a risk to human and ecosystem health. The European Union (EU) and United States Environmental Protection Agency (USEPA) have both recognized CPs as priority contaminants.^{8,9} Nevertheless, the treatment and removal of this class of compounds remains a challenge, wherein the high bond energy of C-Cl (340 kJ mol⁻¹) results in their recalcitrance to conventional biochemical and physicochemical approaches employed in water treatment.¹⁰ Accordingly, the development of efficient dechlorination strategies has received ever-growing attention.

Electrochemical dechlorination has been proposed as an attractive alternative due to the potential to modularize the system, no need for chemical addition, and ease of operation. The key toward attaining a high dechlorination

efficiency is the development of an appropriate electrocatalyst. Among various material options, Pd-based electrocatalysts have been demonstrated to be one of the most effective materials for cathodic dechlorination because Pd can catalyze the Volmer reaction (i.e., $H^+ + e^- \rightarrow H^*$) to generate atomic hydrogen (H^*), a highly reductive species for the substitution of Cl atoms in CPs.^{2,13,14} Much work has been dedicated toward advancing Pd-based electrocatalysts for hydrodechlorination, such as engineering the nanostructures^{15,16} and the inclusion of other elements.^{17–19} Nevertheless, the natural scarcity and high cost of Pd restrict large-scale commercialization, especially in water treatment practices. Moreover, the suitability of conventional Pd-based materials has been questioned as several reports have stated the possibility of

Received: June 29, 2021 Published: September 21, 2021





Pd being poisoned and deactivated by hydrodechlorination by products, namely, chloride. $^{20-22}\,$

Single-atom catalysts (SACs) represent the forefront of advances in catalyst materials and provide an appealing strategy to overcome the intrinsic drawbacks associated with the utilization of noble metals in nanoparticle configuration.^{23–25} Unlike their nanoparticle counterparts, in which a majority of atoms buried under the cluster surface are not involved in catalysis, the atomic dispersion of metal sites enables each atom to be accessible for the target reaction, yielding a theoretical atomic efficiency of 100%. ^{26,27} Another unique characteristic of SACs is an unsaturated coordination environment, affecting their interaction with adsorbates.^{28–30} In particular, adsorbate-induced structural relaxation has been reported to significantly decrease the desorption energy, 28,31,32 which may enable the rapid desorption of Cl- from singleatom Pd (Pd1), mitigating the aforementioned poisoning effect. Despite the success of engineering Pd₁ for many industrially critical reactions (e.g., selective hydrogenation, CO oxidation,³⁴ ammonia electrosynthesis,³⁵ oxygen reduction reaction³⁶), it remains unknown whether the employment of Pd₁ can be an effective catalyst, which outperforms conventional Pd nanoparticles for dechlorination water treatment.

We here report a single-atom Pd electrocatalyst loaded onto a reduced graphene oxide substrate (Pd₁/rGO) for hydrodechlorination. rGO is selected as the electrocatalyst support in this work because it possesses the following: (i) a high specific surface area (up to 2400 m² g⁻¹),³⁷ ensuring the adequate distribution of the active Pd1 sites, and (ii) a superior electrical conductivity (up to $3.0 \times 10^4 \text{ S m}^{-1}$) for fast electron transfer.³⁸ In comparison to graphene (another widely used support for electrocatalysis), rGO contains various oxygencontaining functionalities (i.e., C-OH, -COOH and C=O) on the edge and vacancy defects on the basal plane that can function as anchoring sites and provide a stable coordination environment for SACs. ^{39,40} We evaluate the performance of assynthesized Pd₁/rGO by catalyzing the hydrodechlorination of CPs; detailed material characterizations and mechanistic discussions are presented to reveal the unique role of the single-atom architecture of Pd₁.

■ EXPERIMENTAL

Reagents and Materials. Acetonitrile (C₂H₃N, 99.8% purity), hexane (C₆H₁₄, 97.5% purity), and palladium chloride (PdCl₂, 5 wt % in 10 wt % HCl solution) were obtained from J&K Scientific. rGO was obtained from Strem Chemicals. Methanol (CH₃OH, 99.9% purity), 5,5-dimethyl-1-pyrroline N-oxide (C₆H₁₁NO, DMPO, 98% purity), phosphoric acid (H₃PO₄, 85% purity), 4-chlorophenol (C₆H₄ClOH, 4-CP, 99% purity), 2,4-dichlorophenol (C₆H₃Cl₂OH, 2,4-DCP, 99% purity), 2,4,6-trichlorophenol (C₆H₂Cl₃OH, 2,4,6-TCP, 98% purity), sodium chloride (NaCl, 99% purity), sodium phosphate dibasic (Na₂HPO₄, 99% purity), sodium phosphate monobasic (NaH₂PO₄, 99% purity), (3-aminopropyl)trimethoxysilane (C9H23NO3Si, APTMS, 97% purity), tertbutyl alcohol (C₄H₁₀O, t-BuOH, 98% purity), palladium oxide (PdO, 99.9% purity), 2-propanol (C₃H₈O, 99.5% purity), palladium chloride (PdCl₂, 99.9% purity), and Nafion 117 (5%) were obtained from Sigma-Aldrich. PdCl₂ (1 g) was dissolved in 20 mL of a solution (14.7 mL of H₂O and 5.3 mL of concentrated HCl) to obtain the PdCl₂ (5 wt % PdCl₂ in 10 wt % HCl, forming PdCl₄²⁻) stock solution, which was further diluted to 10 mM for the subsequent Pd loading. Toray 120

carbon paper (Fuel Cell Store) and glassy carbon (CH Instruments) were used as the electrocatalyst supports. All chemicals used in the experiments were of reagent grade or higher and used as received without further purification. Experimental solutions were prepared using ultrapure water (>18.2 $\mathrm{M}\Omega\mathrm{\cdot cm}$) from a Milli-Q system.

Synthesis of Catalysts. rGO (0.5 g, powder) was first functionalized with amine groups by dispersing it in hexane (250 mL) under ultrasonication for 30 min, followed by the addition of APTMS (2 mL). The obtained rGO-NH₂ was separated by centrifugation, washed three times with ethanol and deionized water, and then dried in the oven at 80 °C. Pd₁/rGO was synthesized by dispersing rGO-NH₂ (80 mg) in deionized water (100 mL) under sonication for 30 min; PdCl₂ solution (1 mL, 10 mM) was subsequently added to the suspension and sonicated for another 30 min. The mixture was then irradiated by the UV light (254 nm, intensity = 7.87 mW/cm²) for an additional 60 min to photoreduce the Pd precursor. The Pd₁/rGO product was finally collected via centrifugation, washed with deionized water, and dried in the oven at 80 °C.

For comparison, Pd nanoparticles (Pd_{nano}/rGO) were prepared via a hydrothermal method. rGO powder (80 mg) was dispersed in 5% ethylene glycol solution. After ultrasonication for 30 min, PdCl₂ (5 mL, 10 mM) was added to the suspension. After sonication for another 30 min, the mixture was sealed into a Teflon container and then heated at 120 °C for 4 h with a heating rate of 10 °C/min. The samples were separated by centrifugation and washed three times with ethanol and deionized water. The final Pd_{nano}/rGO nanocomposites were oven-dried overnight at 80 °C and stored for subsequent experiments.

Preparation of Electrodes. The working electrode was prepared by drop-casting catalyst ink onto the carbon paper surface for degradation experiments and the glassy carbon electrode for electrochemical characterization. Pd_1/rGO or Pd_{nano}/rGO (0.8 mg) was mixed with 1.0 mL of 2-propanol, 0.7 mL of deionized water, and 24 μ L of Nafion 117 solution and sonicated for 60 min. Afterward, the homogeneous ink suspension was pipetted onto both substrates under an infrared heat lamp for 60 min and tested immediately. Across all electrochemical experiments, the total catalyst mass loadings of both Pd_1/rGO and Pd_{nano}/rGO were kept the same.

Electrocatalyst Characterization. Aberration-corrected high-angle annular dark-field scanning transmission electron microscopy (AC-HAADF-STEM) was conducted on a JEM-ARM 200F operated at 300 kV. The high-resolution transmission electron microscopy images were obtained using an FEI Tecnai Osiris 200 kV TEM. X-ray powder diffraction (XRD) was taken to examine the phase structure using an X'Pert Pro MPD (PANalytical) with Cu K α radiation. The scan rate was 5°/min within the 2θ range of $10-80^\circ$. X-ray photoelectron spectroscopy (XPS) analysis was conducted using a PHI VersaProbe II Scanning XPS Microprobe system with monochromatic Al K α radiation (1486.6 eV). Raman spectroscopy (LabRAM HR Evolution, Horiba) was performed to observe the characteristic D and G bands of rGObased catalysts. Inductively coupled plasma mass spectrometry (ICP-MS) was performed using a PerkinElmer SCIEX Elan DRC-e to determine the loading of Pd on rGO. The X-ray absorption fine structure (XAFS) spectra at the Pd K-edge were recorded at Beamline 8-ID of the National Synchrotron Light Source II at Brookhaven National Laboratory. The

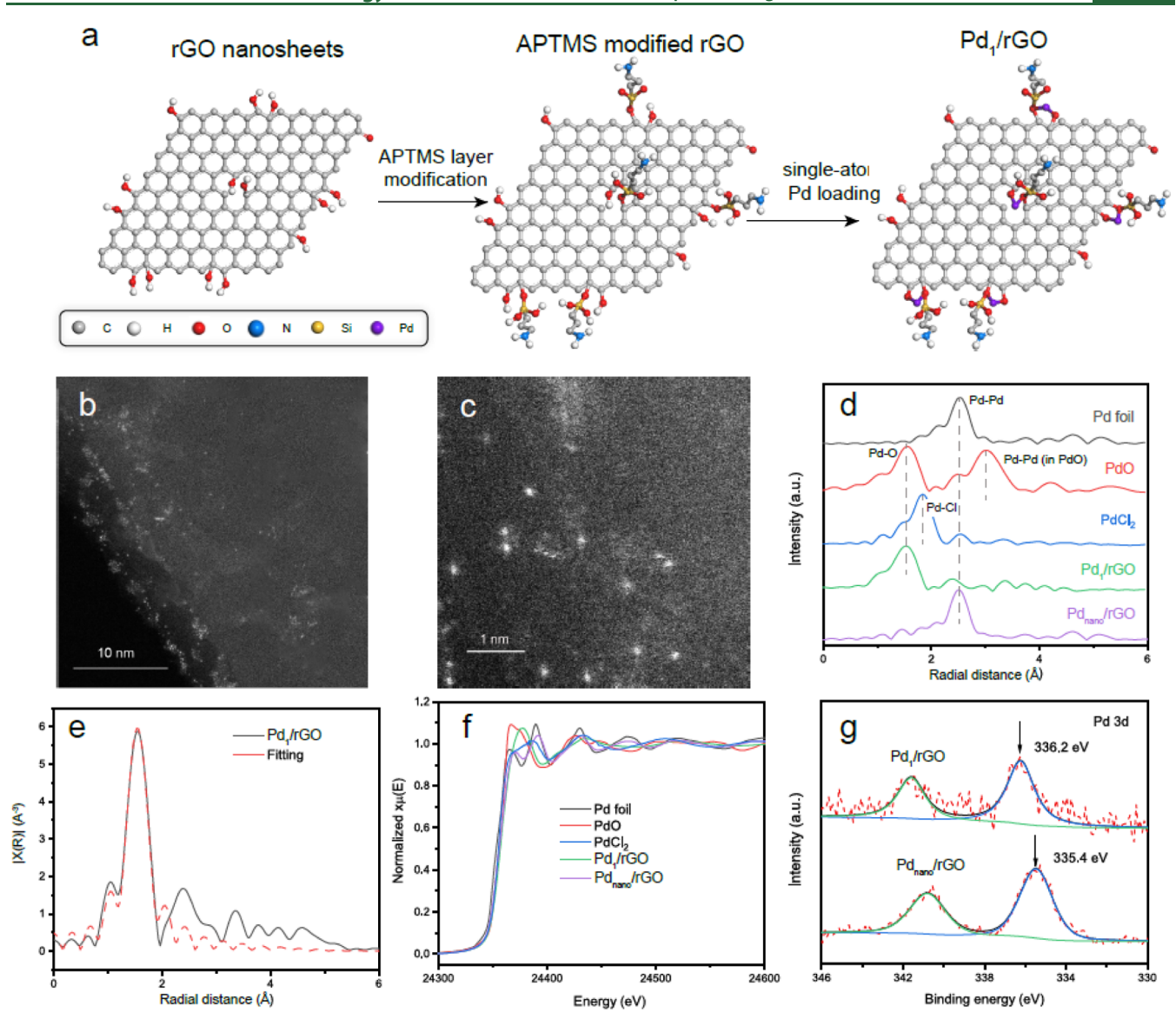


Figure 1. (a) Schematic illustration of the step-by-step synthesis procedure for Pd_1/rGO ; (b,c) AC-HAADF-STEM images of Pd_1/rGO ; (d) Pd K-edge Fourier-transformed extended X-ray absorption fine structure spectroscopy (FT-EXAFS) of Pd foil, PdO, $PdCl_2$, Pd_1/rGO , and Pd_{nano}/rGO ; (e) fitting results for Pd_1/rGO (the parameters extracted from the fit are provided in Table 1); (f) normalized X-ray absorption near-edge structure (XANES) measurements of Pd foil, PdO, $PdCl_2$, Pd_1/rGO , and Pd_{nano}/rGO . The data ranges used for data fitting in the K-space and R-space (Figure S6) were 3.0-12 Å $^{-1}$ and 1.2-2.5 Å, respectively; (g) Pd 3d XPS spectra of Pd_1/rGO and Pd_{nano}/rGO .

energy was calibrated with a Pd foil. The sample was pressed into a pellet and sealed in Kapton films. The data were obtained at room temperature under the fluorescence mode using a passivated implanted planar silicon detector and analyzed by Athena software (Text S1).

Electrochemical Experiments. The cathodic hydrodechlorination of CPs (i.e., 4-CP, 2,4-DCP, 2,4,6-TCP) was conducted using a three-electrode electrochemical cell, where the anodic and cathodic rooms were separated by a Nafion 117 membrane (Figure S1). The volume of each room was 5 mL; the distance between the anode and cathode was 20 mm; the surface areas of Pd-loaded rGO electrodes and the Pt foil were all 2 cm² (10×20 mm). Phosphate buffer (100 mM) was chosen as the electrolyte to avoid drastic pH variation during the reaction. The anodic room was filled with phosphate, and the cathodic room was additionally spiked with CPs. Pd-loaded rGO electrodes were used as the working electrodes; the Pt foil and an Ag/AgCl electrode were used as the counter and

reference electrodes, respectively. All experiments were performed in batch mode at a constant potential of $-1.2 \ V_{\rm Ag/AgCl}$ under stirring at 800 rpm. All electrochemical measurements were conducted and recorded using a SP-50 potentiostat (Bio-Logic).

Analytical Methods. Chlorophenol concentrations were measured in triplicate using high-performance liquid chromatography (HPLC, Agilent Technologies 1260 Infinity) equipped with a C18 column (4.6 mm \times 250 mm, 5 μ m). 4-CP was detected based on absorption at 225 nm; the mobile phase consisted of a 45:55 (v/v) mixture of acetonitrile and phosphoric acid (0.1 wt %) with a flow rate of 2 mL/min. 2,4-DCP was detected based on absorption at 225 nm; the mobile phase consisted of a 50:50 (v/v) mixture of acetonitrile and phosphoric acid (0.1 wt %) with a flow rate of 2 mL/min. 2,4,6-TCP was detected based on absorption at 205 nm; the mobile phase consisted of a 60:40 (v/v) mixture of acetonitrile and phosphoric acid (0.1 wt %) with a flow rate of 2 mL/min.

Electron paramagnetic resonance (EPR) analyses were conducted with an ESR-300E spectrometer (Bruker Instruments) using DMPO as a spin-trapping agent for H*. The concentration of Cl was determined via ion chromatography (IC, Dionex ICS-1100) equipped with Dionex IonPac AS11-HC Analytical and AG11-HC Guard columns. NaCl standard solution was used to calibrate the peak area in relation to Clconcentration.

RESULTS AND DISCUSSION

Synthesis and Structural Characterization of Pd₁/ rGO. As shown in Figure 1a, we applied a two-step method consisting of APTMS modification and photoreduction of the Pd precursor in sequence. The first step involved the interaction of APTMS with OH groups on the edge of rGO, introducing amine functionalities onto rGO (Figures S2 and S3). Amine groups in APTMS converted into positively charged ammonium groups (NH₄⁺) in the aqueous solution. The electrostatic adsorption between NH₄⁺ and negatively charged PdCl₄²⁻ subsequently enabled the distribution of Pd precursors onto the rGO support. APTMS was selected as the organic linker to chelate the Pd precursor because it has demonstrated the ability to additionally tune the electronic structure of metals. 41,42 Notably, even though graphene oxide (GO) generally has more oxygen functionalities for APTMS modification, the high density of such functionalities leads to a low electrical conductivity. 43 Therefore, GO was not selected as the support for the Pd1 electrocatalyst. The second step involved the photoreduction of the Pd precursor by photogenerated electrons under 254 nm UVC irradiation, similar to our previous work.^{23,41,44} This facile process yielded Pd₁/rGO with a Pd loading amount of 0.96 wt % according to ICP-MS results (i.e., Pd/C atomic ratio = 1/830. See Text S2 for calculations). The peaks at 1325, 1580, and 2650 cm⁻¹ observed in Raman spectra (Figure S4) are assigned to D, G, and 2D bands of rGO; a negligible variation between rGO and Pd₁/rGO indicates that Pd₁ loading would not affect the graphitic structure.

The atomic dispersion of Pd on the rGO edge was visually verified as scattered bright spots with a diameter of approximately 2 Å in AC-HAADF-STEM images (as shown in Figure 1b,c). We found a small fraction of Pd₁ anchored on the basal plane of rGO, where structural defects containing -OH groups can react with APTMS and generate spots for the Pd₁ stabilization. 45,46 The absence of the Pd-Pd shell in the FT-EXAFS result of Pd₁/rGO (Figure 1d) confirmed that Pd nanoparticles (Figure S5) did not form. This result is consistent with our XRD results, in which no characteristic peaks of Pd_{nano}/rGO are detected in the Pd₁/rGO sample (Figure S6).

The absence of Pd-Cl demonstrated that chlorine in the PdCl₂ precursor was completely removed during the photoreduction step. Moreover, comparing Pd₁/rGO to the PdO reference (Figure 1d) further validated the Pd-O coordination, which is estimated to be at an interatomic distance of 1.6 Å (Figure 1e). Best-fit parameters extracted from FT-XAFS data (Table 1) suggest that the Pd-O coordination number in Pd₁/rGO is ~3 (in contrast to 4 for PdO), confirming the unsaturated coordination environment of Pd1. The coordinatively unsaturated metal atom, regarded as a critical advantage of SACs, has been proven to promote the adsorption of reactants and thereby improve the catalytic efficiency toward multiple reactions (e.g., Cu₁ for CO oxidation, ⁴⁷ Pt₁ for H₂

Table 1. Best-Fit Parameters Extracted from the Pd K-Edge FT EXAFS Spectra of Pd₁/rGO and Pd_{nano}/rGO^a

sample	shell	CN	R/Å	$\sigma^2/{ m \AA}^2$
PdO	Pd-O	4	2.05	0.0011 ± 0.0007
Pd foil	Pd-Pd	12	2.79	0.0047 ± 0.0006
Pd ₁ /rGO	Pd-O	3.4 ± 0.4	2.04 ± 0.02	0.0013 ± 0.0007
Pd_{nano}/rGO	Pd-Pd	8.2 ± 0.5	2.76 ± 0.01	0.0064 ± 0.004

^aCN is the coordination number of Pd-O or Pd-Pd spheres, R refers to interatomic distances, and σ^2 is the Debye Waller factor.

evolution, 48 Ir₁ for O₂ evolution 49). The interfacial Pd-O bonds can additionally function as the channels for electron transfer between Pd and the rGO support, which have been widely reported as the electronic metal-support interactions (EMSI) that enhance the catalytic reaction. 50-52 The XANES curves (Figure 1f) suggest that the white line intensity of Pd₁, a quantitative indication of the oxidation state, is much higher than Pd⁰ in the Pd foil and Pd_{nano} and close to the Pd²⁺ in the PdO reference. This result is consistent with XPS data, where the $Pd-3d_{5/2}$ binding energy of Pd_1 is 336.2 eV, higher than 335.4 eV of Pd_{nano} and close to 336.4 eV of PdO.⁵³ An oxidation state of \sim 2+ indicates the highly vacant 5d orbitals of Pd₁, and such electron-deficient nature of SACs has been reported to be able to reduce the activation barrier in many important catalyses (e.g., Pt₁ for CO oxidation, ⁵⁴ Fe₁ for benzene oxidation, 55 Ni₁ for CO₂ reduction, 56 Pt₁ for H₂ evolution⁴⁸).

Kinetics of 4-CP Electroreduction. As shown in Figure 2a, Pd₁/rGO exhibited a superior performance over Pd_{nano}/ rGO toward 4-CP reduction, where the pseudo-first-order rate constant (k_{4-CP}) increased by over 3 times from 0.49 ± 0.02 to $1.61 \pm 0.04 \text{ h}^{-1}$. To further evaluate the activity of Pd₁/rGO versus Pd_{nano}/rGO, we calculated the turnover number (TON, Text S2) per Pd atom basis to exclude the contribution from the higher Pd loading in Pd_{nano}/rGO (i.e., 0.96 wt % Pd in Pd₁/rGO and 5.2 wt % in Pd_{nano}/rGO). As shown in the inset of Figure 2a, the TON of Pd₁/rGO is 14 times that of Pd_{nano}/ rGO for 4-CP reduction, indicating a much higher atomic efficiency of Pd in Pd₁/rGO. Given that only surface Pd atoms participate in the reaction, we additionally calculate the TON' of Pd by normalizing based only on the surface Pd atom ratio (Text S2). TON' of Pd₁/rGO remains 4 times that of Pd_{nano}/ rGO, demonstrating the intrinsically higher activity of Pd₁ compared to surface Pd atoms in Pd_{nano}. Under lower pH conditions, Pd₁/rGO yielded higher 4-CP reduction kinetics (Figure 2b), with k_{4-CP} further increasing to 2.92 \pm 0.08 h⁻¹ at pH 5. Considering that the p K_a of 4-CP is 9.41, ⁵⁷ 4-CP would remain neutral in an acidic environment, excluding the enhanced adsorption and subsequent direct cathodic reduction of 4-CP onto Pd₁/rGO. The increased kinetics are ascribed to the promoted indirect cathodic reduction by H*, wherein the higher concentration of H+ could promote H* generation via the Volmer reaction. The kinetics changed negligibly after 20 cycles over 20 h of operation (Figure 2c), demonstrating the high stability of Pd₁/rGO. Moreover, this electrode also exhibited high dechlorination activity for other chlorinated phenols (i.e., 2,4-DCP and 2,4,6-TCP), as presented in Figure

Chlorine mass balances performed throughout the reaction provided insight into the nature of the observed dechlorination reactions. As shown in Figure 3a, the chlorine mass balance was continuously over 95% during 4-CP reduction, where the

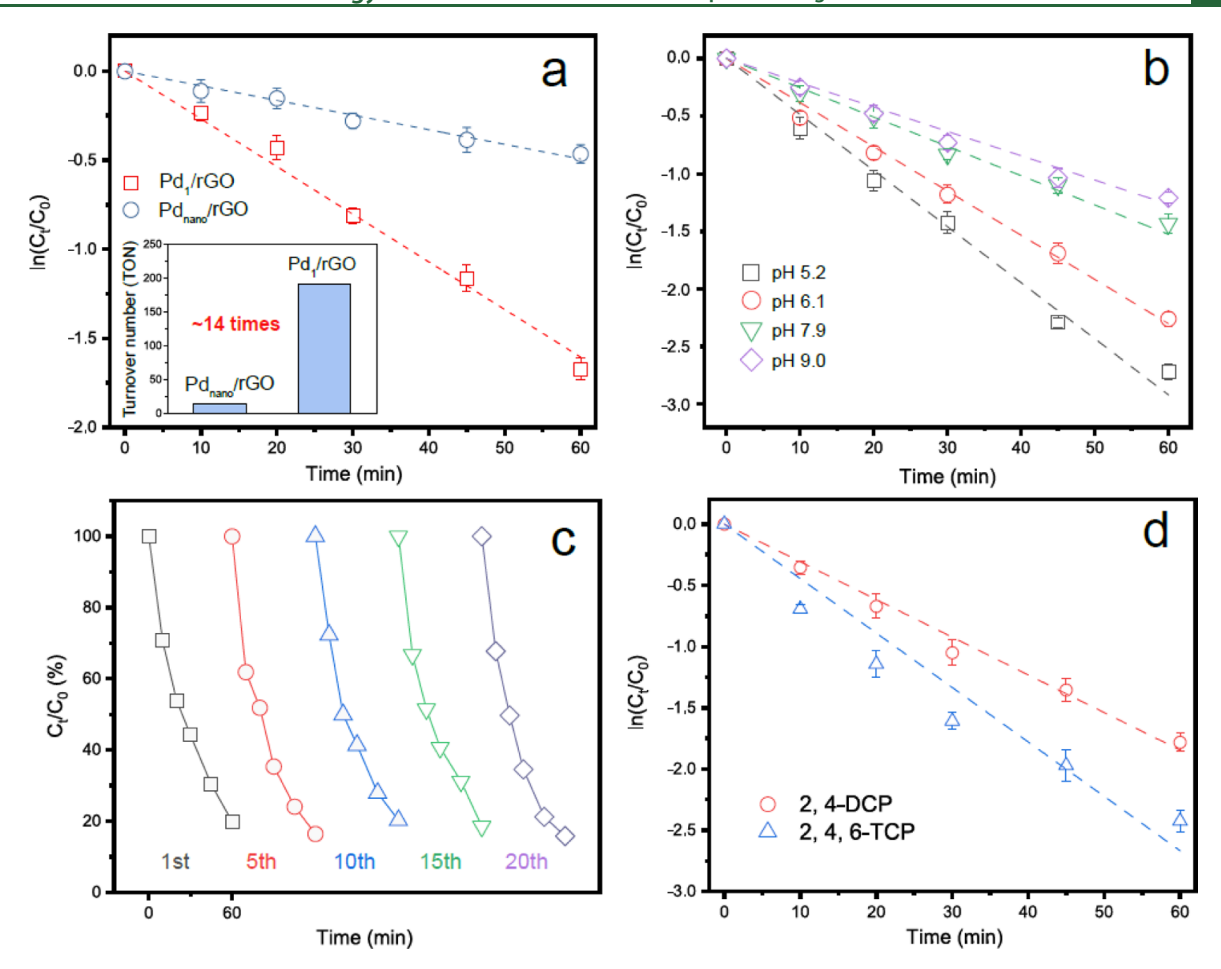


Figure 2. (a) Pseudo-first-order kinetic plots of 4-CP dechlorination with Pd_1/rGO and Pd_{nano}/rGO electrodes. The inset indicates the TON per Pd atom basis in a reaction time of 30 min. (b) 4-CP dechlorination with the Pd_1/rGO cathode under different pH values (5.2, 6.1, 7.9, 9.0); (c) 4-CP dechlorination with the Pd_1/rGO cathode after repetitive cycling. After each cycle, the electrode was washed with methanol and deionized water and then directly subjected to the next cycle. The total run time was 20 h. (d) Pseudo-first-order kinetic plots of 2,4-DCP and 2,4,6-TCP with the Pd_1/rGO cathode. Conditions: potential = -1.2 $V_{Ag/AgCJ}$, CP concentration = 0.1 mM, electrolyte = 100 mM phosphate buffer, pH = \sim 7, temperature = 25 ± 1 °C.

remaining 5% could be attributed to Cl⁻ adsorption onto rGO at the positively charged amine groups. For the reduction of 2,4-DCP and 2,4,6-TCP (Figure 3b,c), slightly lower Cl mass balances during the reaction are observed (88% at 30 min and 90% at 10 min during 2,4-DCP and 2,4,6-TCP reduction, respectively). This might be due to the generation of partially dechlorinated intermediates, given additional C–Cl bonds in the parent compounds. Nevertheless, across all reduction reactions, phenol is the sole detected product, indicating the high selectivity of Pd₁/rGO without dehydroxylation or further hydrogenation of the benzene ring to produce cyclohexanol or cyclohexanone.

Electrochemical Properties of Pd_1/rGO . We performed cyclic voltammetry (CV) scans under various conditions to probe the reasons for the high activity of Pd_1/rGO . Upon the inclusion of 4-CP into the electrolyte, the CV of Pd_1/rGO exhibited a reversible wave centered around 0.35 $V_{Ag/AgCl}$ (Figure 4a, red trace). This has been attributed to the one-electron reversible transformation between the phenolate anion and phenoxyl radical, confirming the hydrodechlorination of 4-CP into phenol. S8,59 The addition of 4-CP led to a striking increase in the reductive current (from -0.50 to -1.20 $V_{Ag/AgCl}$) and a reductive peak at -0.95 $V_{Ag/AgCl}$. Since the

latter feature was not present in pristine phosphate buffer, we allude this to the direct cathodic reduction of 4-CP. 60

Pd₁/rGO displayed the oxidation peak for H* at around 0 V_{Ag/AgCl} (Figure 4a), indicating the occurrence of the Volmer reaction $(H^+ + e^- \rightarrow H^*)$ during the cathodic sweep. ¹⁶ We further investigated this mechanistic behavior of Pd₁/rGO by conducting a series of CVs at various ending potentials (Figure 4b). An increase in the peak height for H* was observed at more negative ending potentials (-0.8 to -1.0 $V_{Ag/AgCl}$); this suggests that higher cathodic currents yield higher amounts of H*. At less reductive potentials (-0.4 to -0.6 $V_{Ag/AgCl}$) in which H* was not observed, the pair of peaks for the phenolate/phenoxyl radical was also not present. In fact, this pair was visible only after applying more negative potentials and upon the emergence of the H* peak. This highlights the role of H* as an active reactant for hydrodechlorination, which has been reported for Pd nanoparticles.^{61,62} Overall, Figure 4a,b demonstrates that both pathways, direct cathodic reduction and indirect hydrogenation involving H*, are involved for 4-CP hydrodechlorination on Pd₁/rGO.

 Pd_1/rGO was further compared to Pd_{nano}/rGO by performing CV at the same total catalyst mass loading (Figure 4c). First, the reductive current for 4-CP hydrodechlorination was far more pronounced for Pd_1/rGO than Pd_{nano}/rGO , despite

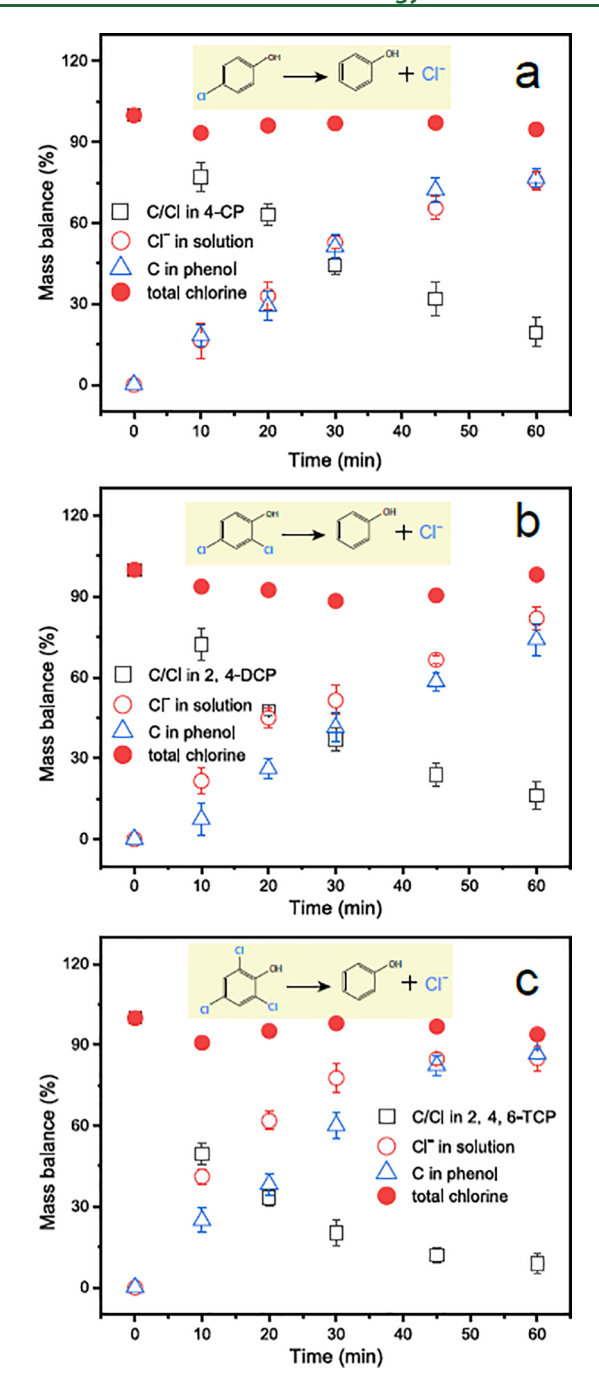


Figure 3. Chlorine mass balances during the (a) 4-CP, (b) 2,4-DCP, and (c) 2,4,6-TCP hydrodechlorination with the Pd $_1$ /rGO electrode. Conditions: potential = $-1.2~V_{Ag/AgCl}$, CP concentration = 0.1 mM, electrolyte = 100 mM phosphate buffer, pH = \sim 7, temperature = 25 \pm 1 °C.

the lower amount of Pd available. We ascribe this observation to the EMSI effect of SACs. Specifically, the strong EMSI between Pd₁ and the rGO support through Pd–O bonds facilitates electron transfer from the underlying rGO support to 4-CP through active Pd₁ sites. We also observed that the H* peak for Pd_{nano}/rGO exposed to 4-CP was much lower than that for Pd₁/rGO and Pd_{nano}/rGO in pristine phosphate buffer (Figure S8). One reason may be the suppression of the Volmer reaction, given the lower reductive currents for Pd_{nano}/rGO. Also, it is possible that H* is better utilized for 4-CP hydrodechlorination; however, this is not in agreement with

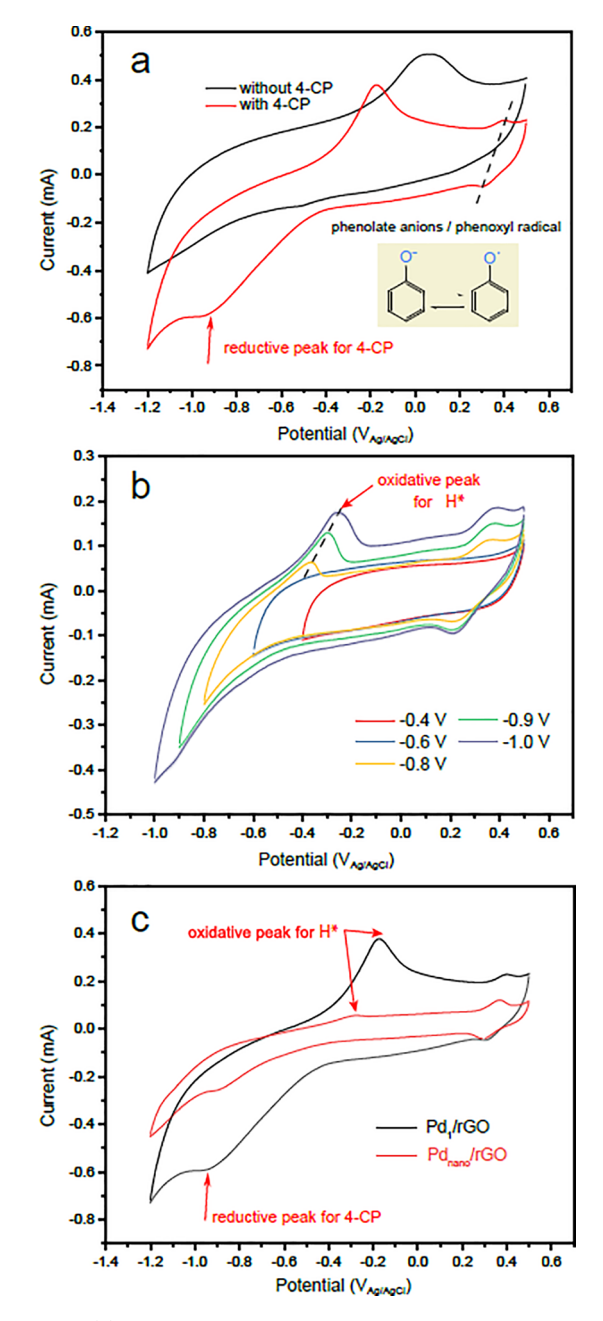


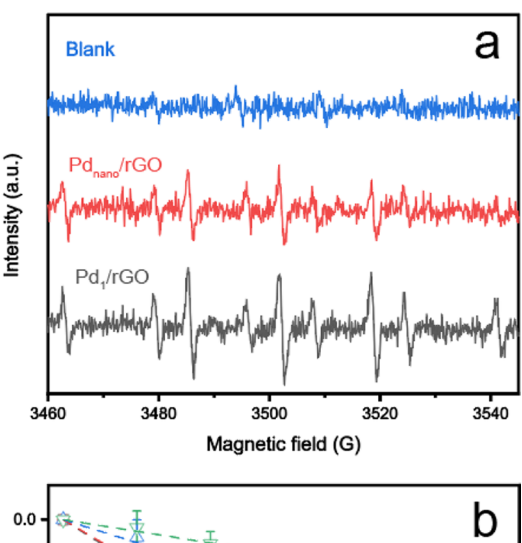
Figure 4. (a) CV curves of Pd_1/rGO in the electrolyte with and without addition of 4-CP; (b) effect of different ending potential limits on Pd_1/rGO with 4-CP. Starting potentials were fixed at 0.5 $V_{Ag/AgCl}$; (c) cyclic voltammograms of Pd_1/rGO and Pd_{nano}/rGO in the electrolyte with 4-CP; CV of Pd_1/rGO is the duplication of "with 4-CP" in Figure 4a. The mass loading of the catalyst was kept the same for both Pd_1/rGO and Pd_{nano}/rGO at 0.016 mg/cm^2 . Conditions: electrolyte = 100 mM phosphate buffer (N_2 -saturated), pH = 7, 4-CP concentration = 5 mM, scan rate = 50 mV/s, temperature = 25 ± 1 °C.

the lower dechlorination kinetics of Pd_{nano}/rGO compared to Pd_1/rGO (Figure 2a). In fact, 4-CP dechlorination kinetics for Pd_{nano}/rGO continuously decreased over time (Figure S9), unlike Pd_1/rGO , in which kinetics were maintained under the same conditions even after 20 h (Figure 2c). Therefore, 4-CP or its byproducts impeding the ability of Pd_{nano}/rGO to produce H^* might be another reason for the decrease in overall dechlorination efficiency.

One major limitation of Pd-based catalysts is poisoning by the reaction byproducts. 64-67 Previous studies reported that the presence of chloride could hinder the activity of these catalysts via strong adsorption onto the Pd surface, blocking the active sites from additional reactants.⁶⁸⁻⁷⁰ As shown in Figure S10, Pd_{nano}/rGO demonstrates substantial losses in reductive current after cycling in the 4-CP-containing electrolyte, whereas Pd₁/rGO exhibits marginal changes under the same conditions. To further investigate, we conducted separate stability tests with Pd₁/rGO and Pd_{nano}/rGO operated at a constant potential in solutions with and without 4-CP (Figures S11 and S12). Although currents were stable for both catalysts in phosphate buffer, the current exhibited by Pd_{nano}/rGO decreased over time upon introduction of 4-CP, which may be caused by the sluggish desorption of resultant Cl- from the Pd_{nano} interface.²¹ This is inferred in Figure S13, in which replacing phosphate buffer with NaCl led to substantial losses in both the H* peak and reductive current. In contrast, Pd₁/ rGO exhibited stable currents throughout the entire reaction time, regardless of the presence of 4-CP. This remarkable stability of Pd₁/rGO was confirmed by performing additional experiments with Pd₁/rGO independently exposed to Cl⁻, phenol, and 2,4-DCP (Figures S14-S16). None of these constituents led to significant losses in the reductive current. Moreover, despite a shift in its location (Text S5), the H* peak was always observed in the cyclic voltammograms, indicating that neither chlorinated phenols nor their dechlorination byproducts detracted from the ability of Pd₁/rGO to continuously produce H*.

Overall, Pd₁/rGO for dechlorination-based processes presents an interesting and promising example of engineering single-atom architectures for water remediation applications. This approach has already been undertaken for various types of catalysts to mitigate such poisoning effects.⁷¹ For example, single-atom Pt and single-atom Ir maintain outstanding performance during CO oxidation, whereas their nanoparticle counterparts are rapidly deactivated due to the strong binding affinity of the CO reactant and subsequent blocking of the surface. 54,72 Similarly, single-atom Cu for electrochemical CO_2 reduction exhibits superb resistance to methanol poisoning, which is attributed to its weaker binding, in comparison to Cu nanoparticles.⁷³ Such decreased binding affinities have been attributed to the adsorbate-induced structural relaxation of SACs, wherein the unsaturated coordination environment enables the distortion of the SAC structure to affect the desorption of the intermediate. 28,31,32 Combining these previous findings and our experimental results, we propose that the superior catalytic stability of Pd₁/rGO over Pd_{nano}/ rGO for 4-CP hydrodechlorination results from its single-atom

Role of H*. EPR analysis using DMPO as the probe (Figure 5a) displayed a series of nine characteristic peaks for both Pd₁/rGO and Pd_{nano}/rGO, corresponding to the presence of H*. Although the relative intensities of the DMPO/H* adducts of each test could not provide a quantitative correlation, a stronger intensity can generally be qualitatively interpreted as a higher concentration of H*,^{60,74} where the stronger signal for Pd₁/rGO confirms the enhanced H* formation. To further understand the contribution from H* versus direct cathodic reduction, we additionally performed quenching experiments for H* using *t*-BuOH. The reaction pathways are shown in eqs 1 and 2^{75,76}



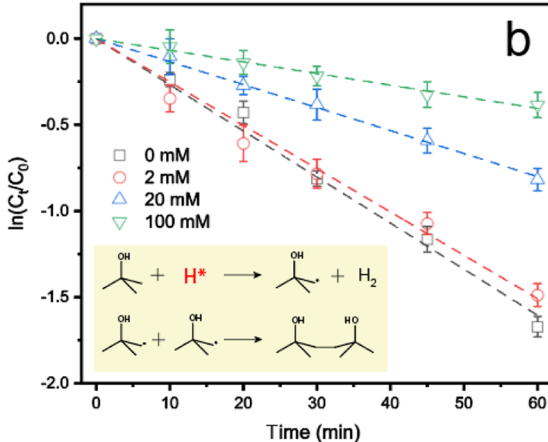


Figure 5. (a) EPR spectra of the blank, Pd_1/rGO , and Pd_{nano}/rGO with DMPO as the probe; (b) 4-CP hydrodechlorination on the Pd_1/rGO cathode with the different concentrations of t-BuOH, which acts as the quenching agent for H*. 0 mM is the duplication of the Pd_1/rGO curve in Figure 2b. Conditions: potential = $-1.2~V_{Ag/AgCl}$, 4-CP concentration = 0.1 mM, electrolyte = 100 mM phosphate buffer, pH = \sim 7, temperature = $25 \pm 1~^{\circ}C$.

$$(CH_3)_3COH + H^*$$

 $\rightarrow {}^{\bullet}CH_2(CH_3)_2COH + H_2(k_1$
 $= 7.5 \times 10^7 M^{-1} s^{-1})$ (1)

$${}^{\bullet}\text{CH}_{2}(\text{CH}_{3})_{2}\text{COH} + {}^{\bullet}\text{CH}_{2}(\text{CH}_{3})_{2}\text{COH}\text{products} (k_{2})$$

= $(1.23 \pm 0.3) \times 10^{9} \,\text{M}^{-1}\text{s}^{-1})$ (2)

As shown in Figure 5b, increasing the concentration of t-BuOH in the electrolyte led to sharp decreases in $k_{4\text{-CP}}$, dropping to $0.41 \pm 0.01 \text{ h}^{-1}$ at 100 mM t-BuOH ($\sim 1/4$ the value of $k_{4\text{-CP}}$ in pristine phosphate buffer). This underscores the active role of H* in the dechlorination process and is consistent with the data presented in Figure 2c. Specifically, the Volmer reaction becomes kinetically favorable with the increase in proton concentration, generating more H* and leading to an increase in $k_{4\text{-CP}}$ at lower pH values. However, 4-CP hydrodechlorination did not cease even under an extremely high t-BuOH concentration of 100 mM, indicating the cocontribution from direct cathodic reduction. We caution quantitative analysis based on the kinetics; the large amount of t-BuOH may also affect surface interactions between the

electrode and 4-CP, reflected by lower reductive currents (Figure S18).

Environmental Significance. As shown in Figure 6, the superior catalytic performance of Pd₁/rGO toward 4-CP

Increased H* utilization efficiency due to the inhibited H2 evolution.



Figure 6. Proposed mechanism of enhanced cathodic hydrodechlorination with Pd_1/rGO versus Pd_{nano}/rGO .

hydrodechlorination is attributed to characteristic properties that emerge as Pd is engineered to be at the atomic scale. Interfacial Pd-O bonds can function as a channel for electron transfer from the rGO support to adsorbed 4-CP; this EMSI effect promotes the direct cathodic reduction of 4-CP. When Pd₁ is occupied by the adsorbed proton, the EMSI effect could enhance the electron transfer from rGO to the proton (i.e., Volmer reaction) as well, generating more H* as reactive species for the indirect hydrogenation of 4-CP. Notably, as calculated in the previous study, the competitive H2 evolution reaction (HER) usually consumes most of H* during the electrocatalytic hydrodechlorination with conventional Pd nanomaterials, leading to a low H* utilization efficiency of 10-30%.²¹ Suppressing HER has thus become an efficient strategy to boost the hydrodechlorination rates. Given the limited adsorption sites on the single-atom architecture, H* generated from the Volmer reaction could block the Pd₁ surface⁷⁷ and thus hinder the subsequent adsorption of a second proton, which is necessary for HER via the Heyrovsky step $(H^* + H^+ + e^- \rightarrow H_2)$. As for the Tafel step, another pathway for HER, the spatial separation of Pd atoms in Pd₁/ rGO would suppress the rapid recombination of two H* generated on adjacent Pd atoms (H* + H* \rightarrow H₂), a wellknown phenomenon that takes place on the Pdnano surface. The enhanced EMSI effect and inhibited competitive HER result in a much higher Pd atomic efficiency of Pd₁/rGO, which is 14 times that of Pd_{nano}/rGO according to the TON calculation. For example, 0.6 mg of Pd₁ can dechlorinate 1 mmol of 4-CP within 30 min, while 8.4 mg of Pdnano is required to achieve the same dechlorination effect. We have also experimentally demonstrated the stability of Pd₁/rGO, which is able to resist Cl deactivation that has been noted for its nanoparticle counterparts. 25,26 Further developments on loading Pd₁/rGO onto porous conductive supports instead of carbon paper may enable the design of a flow-through system, increasing kinetics and energy efficiency by alleviating mass-transfer limitations.

ASSOCIATED CONTENT

5 Supporting Information

The Supporting Information is available free of charge at https://pubs.acs.org/doi/10.1021/acs.est.1c04294.

XAFS data fitting, calculations of Pd atom efficiency, phosphate buffer preparation, acid treatment of carbon paper, shifts in the H* peak; schematic of the three-electrode electrocatalytic system; supplementary characterizations of XPS, XRD, Raman spectroscopy, and high-resolution transmission electron microscopy; recycling experiments; CV under different conditions; and long-term chronoamperometry experiments (PDF).

AUTHOR INFORMATION

Corresponding Authors

Junfeng Niu — Research Center for Eco-environmental Engineering, Dongguan University of Technology, Dongguan, Guangdong 523808, P. R. China; ⊚ orcid.org/0000-0003-2592-3103; Phone: +86-769-22863180; Email: niujf@dgut.edu.cn; Fax: +86-769-22863180

Jae-Hong Kim — Department of Chemical and Environmental Engineering, Yale University, New Haven, Connecticut 06520, United States; NSF Nanosystems Engineering Research Center for Nanotechnology Enabled Water Treatment (NEWT), Yale University, New Haven, Connecticut 06511, United States; ○ orcid.org/0000-0003-2224-3516; Phone: +1-203-432-4386; Email: jaehong.kim@yale.edu; Fax: +1-203-432-4387

Authors

Dahong Huang — Research Center for Eco-environmental Engineering, Dongguan University of Technology, Dongguan, Guangdong 523808, P. R. China; Department of Chemical and Environmental Engineering, Yale University, New Haven, Connecticut 06520, United States; orcid.org/0000-0003-4544-6113

David J. Kim – Department of Chemical and Environmental Engineering, Yale University, New Haven, Connecticut 06520, United States

Kali Rigby — Department of Chemical and Environmental Engineering, Yale University, New Haven, Connecticut 06520, United States; orcid.org/0000-0002-4582-2388

Xuechen Zhou – Department of Chemical and Environmental Engineering, Yale University, New Haven, Connecticut 06520, United States

Xuanhao Wu — Department of Chemical and Environmental Engineering, Yale University, New Haven, Connecticut 06520, United States; orcid.org/0000-0001-6177-6089

Aidan Meese – Department of Chemical and Environmental Engineering, Yale University, New Haven, Connecticut 06520, United States

Eli Stavitski – National Synchrotron Light Source-II, Brookhaven National Laboratory, New York, New York 11973, United States

Complete contact information is available at: https://pubs.acs.org/10.1021/acs.est.1c04294

Author Contributions

"These authors contributed equally.

Notes

The authors declare no competing financial interest.

ACKNOWLEDGMENTS

This study was financially supported by the National Science Fund for Distinguished Young Scholars (no. 51625801), the National Natural Science Foundation of China (no. 51878169), the Guangdong Innovation Team Project for Colleges and Universities (no. 2016KCXTD023), and the Guangdong Province Universities and Colleges Pearl River Scholar Funded Scheme (2017). This study was partly supported the National Science Foundation (NSF) Nanosystems Engineering Research Center for Nanotechnology-Enabled Water Treatment (EEC-1449500) and NSF Division of Chemical, Bioengineering, Environmental, and Transport Systems (CBET) grant #1955793. This research used beamline 8-ID (Inner Shell Spectroscopy, ISS) of the National Synchrotron Light Source II, a U.S. Department of Energy (DOE) Office of Science User Facility operated for the DOE Office of Science by Brookhaven National Laboratory under contract no. DE-SC0012704.

REFERENCES

- (1) Yang, X.; Ou, W.; Xi, Y.; Chen, J.; Liu, H. Emerging polar phenolic disinfection byproducts are high-affinity human transthyretin disruptors: an in vitro and in silico study. *Environ. Sci. Technol.* **2019**, 53, 7019–7028.
- (2) Jiang, G.; Lan, M.; Zhang, Z.; Lv, X.; Lou, Z.; Xu, X.; Dong, F.; Zhang, S. Identification of active hydrogen species on palladium nanoparticles for an enhanced electrocatalytic hydrodechlorination of 2,4-dichlorophenol in water. *Environ. Sci. Technol.* **2017**, *51*, 7599–7605
- (3) Zhou, T.; Li, Y.; Ji, J.; Wong, F.-S.; Lu, X. Oxidation of 4-chlorophenol in a heterogeneous zero valent iron/H₂O₂ Fenton-like system: Kinetic, pathway and effect factors. *Sep. Purif. Technol.* **2008**, 62, 551–558.
- (4) Igbinosa, E. O.; Odjadjare, E. E.; Chigor, V. N.; Igbinosa, I. H.; Emoghene, A. O.; Ekhaise, F. O.; Igiehon, N. O.; Idemudia, O. G. Toxicological profile of chlorophenols and their derivatives in the environment: the public health perspective. *Sci. World J.* **2013**, 2013, 460215.
- (5) Besser, J. M.; Wang, N.; Dwyer, F. J.; Mayer, F. L.; Ingersoll, C. G. Assessing contaminant sensitivity of endangered and threatened aquatic species: Part II. Chronic toxicity of copper and pentachlorophenol to two endangered species and two surrogate species. *Arch. Environ. Contam. Toxicol.* **2005**, 48, 155–165.
- (6) Cooper, G. S.; Jones, S. Pentachlorophenol and cancer risk: focusing the lens on specific chlorophenols and contaminants. *Environ. Health Perspect.* **2008**, *116*, 1001–1008.
- (7) Tisch, M.; Bergenthal, S.; Maier, H. Genotoxic effect of PCP and lindane on human epithelial tonsil cells. *HNO* **2002**, *50*, 920–927.
- (8) US Environmental Protection Agency. Edition of the Drinking Water Standards and Health Advisories; US Environmental Protection Agency: Washington, DC, epa 2006.
- (9) European Environment Agency. Progress in Management of Contaminated Sites; European Environment Agency: Copenhagen, 2007, Online Report CSI 015.
- (10) Martin, E. T.; McGuire, C. M.; Mubarak, M. S.; Peters, D. G. Electroreductive remediation of halogenated environmental pollutants. *Chem. Rev.* **2016**, *116*, 15198–15234.
- (11) Rodrigo, M. A.; Oturan, N.; Oturan, M. A. Electrochemically assisted remediation of pesticides in soils and water: a review. *Chem. Rev.* **2014**, *114*, 8720–8745.

- (12) Gan, G.; Li, X.; Wang, L.; Fan, S.; Mu, J.; Wang, P.; Chen, G. Active sites in single-atom $Fe-N_x-C$ nanosheets for selective electrochemical dechlorination of 1, 2-dichloroethane to ethylene. *ACS Nano* **2020**, *14*, 9929–9937.
- (13) Zhou, Y.; Zhang, G.; Ji, Q.; Zhang, W.; Zhang, J.; Liu, H.; Qu, J. Enhanced stabilization and effective utilization of atomic hydrogen on Pd—In nanoparticles in a flow-through electrode. *Environ. Sci. Technol.* **2019**, *53*, 11383—11390.
- (14) Zeng, H.; Zhang, G.; Ji, Q.; Liu, H.; Hua, X.; Xia, H.; Sillanpää, M.; Qu, J. pH-independent production of hydroxyl radical from atomic H*-mediated electrocatalytic H₂O₂ reduction: a green Fenton process without byproducts. *Environ. Sci. Technol.* **2020**, *54*, 14725–14731.
- (15) Jiang, G.; Li, X.; Shen, Y.; Shi, X.; Lv, X.; Zhang, X.; Dong, F.; Qi, G.; Liu, R. Mechanistic insight into the electrocatalytic hydrodechlorination reaction on palladium by a facet effect study. *J. Catal.* **2020**, *391*, 414–423.
- (16) Liu, R.; Zhao, H.; Zhao, X.; He, Z.; Lai, Y.; Shan, W.; Bekana, D.; Li, G.; Liu, J. Defect sites in ultrathin Pd nanowires facilitate the highly efficient electrochemical hydrodechlorination of pollutants by H_{ads}*. *Environ. Sci. Technol.* **2018**, *52*, 9992–10002.
- (17) Zhang, J.; Ji, Q.; Lan, H.; Zhang, G.; Liu, H.; Qu, J. Synchronous reduction—oxidation process for efficient removal of trichloroacetic acid: H* initiates dechlorination and ·OH is responsible for removal efficiency. *Environ. Sci. Technol.* **2019**, *53*, 14586—14594.
- (18) Liu, R.; Chen, H.-m.; Fang, L.-p.; Xu, C.; He, Z.; Lai, Y.; Zhao, H.; Bekana, D.; Liu, J.-f. Au@Pd bimetallic nanocatalyst for carbon—halogen bond cleavage: An old story with new insight into how the activity of Pd is influenced by Au. *Environ. Sci. Technol.* **2018**, *52*, 4244–4255.
- (19) Pretzer, L. A.; Song, H. J.; Fang, Y.-L.; Zhao, Z.; Guo, N.; Wu, T.; Arslan, I.; Miller, J. T.; Wong, M. S. Hydrodechlorination catalysis of Pd-on-Au nanoparticles varies with particle size. *J. Catal.* **2013**, 298, 206–217.
- (20) Heck, K. N.; Nutt, M. O.; Alvarez, P.; Wong, M. S. Deactivation resistance of Pd/Au nanoparticle catalysts for waterphase hydrodechlorination. *J. Catal.* **2009**, *267*, 97–104.
- (21) Fu, W.; Shu, S.; Li, J.; Shi, X.; Lv, X.; Huang, Y.-X.; Dong, F.; Jiang, G. Identifying the rate-determining step of the electrocatalytic hydrodechlorination reaction on palladium nanoparticles. *Nanoscale* **2019**, *11*, 15892–15899.
- (22) Perrone, L.; Prati, L.; Rossi, M. Removal of chlorinated organic compounds from water by catalytic dehydrohalogenation. *Appl. Catal., B* **1998**, *15*, 241–246.
- (23) Huang, D.; de Vera, G. A.; Chu, C.; Zhu, Q.; Stavitski, E.; Mao, J.; Xin, H.; Spies, J. A.; Schmuttenmaer, C. A.; Niu, J.; Haller, G. L.; Kim, J.-H. Single-atom Pt catalyst for effective C—F bond activation via hydrodefluorination. *ACS Catal.* **2018**, *8*, 9353—9358.
- (24) Chu, C.; Yang, J.; Zhou, X.; Huang, D.; Qi, H.; Weon, S.; Li, J.; Elimelech, M.; Wang, A.; Kim, J.-H. Cobalt single atoms on tetrapyridomacrocyclic support for efficient peroxymonosulfate activation. *Environ. Sci. Technol.* **2020**, *55*, 1242–1250.
- (25) Zhou, P.; Li, N.; Chao, Y.; Zhang, W.; Lv, F.; Wang, K.; Yang, W.; Gao, P.; Guo, S. Thermolysis of noble metal nanoparticles into electron-rich phosphorus-coordinated noble metal single atoms at low temperature. *Angew. Chem., Int. Ed.* **2019**, *58*, 14184–14188.
- (26) Peng, M.; Dong, C.; Gao, R.; Xiao, D.; Liu, H.; Ma, D. Fully exposed cluster catalyst (FECC): toward rich surface sites and full atom utilization efficiency. ACS Cent. Sci. 2020, 7, 262–273.
- (27) Weon, S.; Huang, D.; Rigby, K.; Chu, C.; Wu, X.; Kim, J.-H. Environmental materials beyond and below the nanoscale: single-atom catalysts. *ACS ES&T Engg* **2020**, *1*, 157–172.
- (28) Hulva, J.; Meier, M.; Bliem, R.; Jakub, Z.; Kraushofer, F.; Schmid, M.; Diebold, U.; Franchini, C.; Parkinson, G. S. Unraveling CO adsorption on model single-atom catalysts. *Science* **2021**, *371*, 375–379.

- (29) Xi, J.; Jung, H. S.; Xu, Y.; Xiao, F.; Bae, J. W.; Wang, S. Synthesis strategies, catalytic applications, and performance regulation of single-atom catalysts. Adv. Funct. Mater. 2021, 31, 2008318.
- (30) Zhang, Z.; Zhao, X.; Xi, S.; Zhang, L.; Chen, Z.; Zeng, Z.; Huang, M.; Yang, H.; Liu, B.; Pennycook, S. J.; Chen, P. Atomically dispersed cobalt trifunctional electrocatalysts with tailored coordination environment for flexible rechargeable Zn-Air battery and selfdriven water splitting. Adv. Energy Mater. 2020, 10, 2002896.
- (31) Zhang, H.; Li, J.; Xi, S.; Du, Y.; Hai, X.; Wang, J.; Xu, H.; Wu, G.; Zhang, J.; Lu, J.; Wang, J. A Graphene-supported single-atom FeN₅ catalytic site for efficient electrochemical CO₂ reduction. Angew. Chem., Int. Ed. Engl. 2019, 58, 14871-14876.
- (32) Gong, Y. N.; Jiao, L.; Qian, Y.; Pan, C. Y.; Zheng, L.; Cai, X.; Liu, B.; Yu, S. H.; Jiang, H. L. Regulating the coordination environment of MOF-templated single-atom Nickel electrocatalysts for boosting CO2 reduction. Angew. Chem., Int. Ed. 2020, 59, 2705-
- (33) Liu, P.; Zhao, Y.; Qin, R.; Mo, S.; Chen, G.; Gu, L.; Chevrier, D. M.; Zhang, P.; Guo, Q.; Zang, D.; Wu, B.; Fu, G.; Zheng, N. Photochemical route for synthesizing atomically dispersed palladium catalysts. Science 2016, 352, 797-800.
- (34) Xu, H.; Zhang, Z.; Liu, J.; Do-Thanh, C.-L.; Chen, H.; Xu, S.; Lin, Q.; Jiao, Y.; Wang, J.; Wang, Y. Entropy-stabilized single-atom Pd catalysts via high-entropy fluorite oxide supports. Nat. Commun. 2020, 11, 3908.
- (35) Han, L.; Ren, Z.; Ou, P.; Cheng, H.; Rui, N.; Lin, L.; Liu, X.; Zhuo, L.; Song, J.; Sun, J.; Luo, J.; Xin, H. L. Modulating single-atom palladium sites with copper for enhanced ambient ammonia electrosynthesis. Angew. Chem., Int. Ed. 2020, 60, 345-350.
- (36) Xi, J.; Yang, S.; Silvioli, L.; Cao, S.; Liu, P.; Chen, Q.; Zhao, Y.; Sun, H.; Hansen, J. N.; Haraldsted, J.-P. B.; Kibsgaard, J.; Rossmeisl, J.; Bals, S.; Wang, S.; Chorkendorff, I. Highly active, selective, and stable Pd single-atom catalyst anchored on N-doped hollow carbon sphere for electrochemical H2O2 synthesis under acidic conditions. J. Catal. 2021, 393, 313-323.
- (37) Zhang, L. L.; Zhao, X.; Stoller, M. D.; Zhu, Y.; Ji, H.; Murali, S.; Wu, Y.; Perales, S.; Clevenger, B.; Ruoff, R. S. Highly conductive and porous activated reduced graphene oxide films for high-power supercapacitors. Nano Lett. 2012, 12, 1806-1812.
- (38) Moon, I. K.; Lee, J.; Ruoff, R. S.; Lee, H. Reduced graphene oxide by chemical graphitization. Nat. Commun. 2010, 1, 73.
- (39) Xi, J.; Sun, H.; Wang, D.; Zhang, Z.; Duan, X.; Xiao, J.; Xiao, F.; Liu, L.; Wang, S. Confined-interface-directed synthesis of Palladium single-atom catalysts on graphene/amorphous carbon. Appl. Catal., B 2018, 225, 291-297.
- (40) Liang, S.; Zhu, C.; Zhang, N.; Zhang, S.; Qiao, B.; Liu, H.; Liu, X.; Liu, Z.; Song, X.; Zhang, H.; Hao, C.; Shi, Y. A Novel Single-Atom Electrocatalyst Ti1/rGO for Efficient Cathodic Reduction in Hybrid Photovoltaics. Adv. Mater. 2020, 32, 2000478.
- (41) Huang, D.; He, N.; Zhu, Q.; Chu, C.; Weon, S.; Rigby, K.; Zhou, X.; Xu, L.; Niu, J.; Stavitski, E.; Kim, J.-H. Conflicting roles of coordination number on catalytic performance of single-atom Pt catalysts. ACS Catal. 2021, 11, 5586-5592.
- (42) Chu, C.; Huang, D.; Zhu, Q.; Stavitski, E.; Spies, J. A.; Pan, Z.; Mao, J.; Xin, H. L.; Schmuttenmaer, C. A.; Hu, S.; Kim, J.-H. Electronic tuning of metal nanoparticles for highly efficient photocatalytic hydrogen peroxide production. ACS Catal. 2018, 9, 626-
- (43) Gómez-Navarro, C.; Weitz, R. T.; Bittner, A. M.; Scolari, M.; Mews, A.; Burghard, M.; Kern, K. Electronic transport properties of individual chemically reduced graphene oxide sheets. Nano Lett. 2007, 7, 3499-3503.
- (44) Weon, S.; Suh, M.-J.; Chu, C.; Huang, D.; Stavitski, E.; Kim, J.-H. Site-selective loading of single-atom Pt on TiO₂ for photocatalytic oxidation and reductive hydrodefluorination. ACS ES&T Engg 2021, 1, 512-522.
- (45) Chen, X.; Peng, M.; Cai, X.; Chen, Y.; Jia, Z.; Deng, Y.; Mei, B.; Jiang, Z.; Xiao, D.; Wen, X.; Wang, N.; Liu, H.; Ma, D. Regulating coordination number in atomically dispersed Pt species on defect-rich

- graphene for n-butane dehydrogenation reaction. Nat. Commun. 2021, 12, 2664.
- (46) Zhang, L.; Jia, Y.; Gao, G.; Yan, X.; Chen, N.; Chen, J.; Soo, M. T.; Wood, B.; Yang, D.; Du, A.; Yao, X. Graphene defects trap atomic Ni species for hydrogen and oxygen evolution reactions. Chem 2018,
- (47) Yu, W.-Z.; Wang, W.-W.; Li, S.-Q.; Fu, X.-P.; Wang, X.; Wu, K.; Si, R.; Ma, C.; Jia, C.-J.; Yan, C.-H. Construction of active site in a sintered copper-ceria nanorod catalyst. J. Am. Chem. Soc. 2019, 141, 17548-17557.
- (48) Cheng, N.; Stambula, S.; Wang, D.; Banis, M. N.; Liu, J.; Riese, A.; Xiao, B.; Li, R.; Sham, T.-K.; Liu, L.-M.; Botton, G. A.; Sun, X. Platinum single-atom and cluster catalysis of the hydrogen evolution reaction. Nat. Commun. 2016, 7, 13638.
- (49) Zhang, Y.; Wu, C.; Jiang, H.; Lin, Y.; Liu, H.; He, Q.; Chen, S.; Duan, T.; Song, L. Atomic iridium incorporated in cobalt hydroxide for efficient oxygen evolution catalysis in neutral electrolyte. Adv. Mater. 2018, 30, No. e1707522.
- (50) Huang, D.; Wang, K.; Niu, J.; Chu, C.; Weon, S.; Zhu, Q.; Lu, J.; Stavitski, E.; Kim, J.-H. Amorphous Pd-loaded Ti₄O₇ electrode for direct anodic destruction of perfluorooctanoic acid. Environ. Sci. Technol. 2020, 54, 10954-10963.
- (51) Shi, Y.; Ma, Z.-R.; Xiao, Y.-Y.; Yin, Y.-C.; Huang, W.-M.; Huang, Z.-C.; Zheng, Y.-Z.; Mu, F.-Y.; Huang, R.; Shi, G.-Y.; Sun, Y.-Y.; Xia, X.-H.; Chen, W. Electronic metal-support interaction modulates single-atom platinum catalysis for hydrogen evolution reaction. Nat. Commun. 2021, 12, 3021.
- (52) Li, J.; Guan, Q.; Wu, H.; Liu, W.; Lin, Y.; Sun, Z.; Ye, X.; Zheng, X.; Pan, H.; Zhu, J.; Chen, S.; Zhang, W.; Wei, S.; Lu, J. Highly active and stable metal single-atom catalysts achieved by strong electronic metal-support interactions. J. Am. Chem. Soc. 2019, 141, 14515-14519.
- (53) Hu, W.; Li, G.-X.; Chen, J.-J.; Huang, F.-J.; Wu, Y.; Yuan, S.-D.; Zhong, L.; Chen, Y.-Q. Enhanced catalytic performance of a PdO catalyst prepared via a two-step method of in situ reductionoxidation. Chem. Commun. 2017, 53, 6160-6163.
- (54) Qiao, B.; Wang, A.; Yang, X.; Allard, L. F.; Jiang, Z.; Cui, Y.; Liu, J.; Li, J.; Zhang, T. Single-atom catalysis of CO oxidation using Pt₁/FeO_x. Nat. Chem. **2011**, 3, 634-641.
- (55) Deng, D.; Chen, X.; Yu, L.; Wu, X.; Liu, Q.; Liu, Y.; Yang, H.; Tian, H.; Hu, Y.; Du, P.; Si, R.; Wang, J.; Cui, X.; Li, H.; Xiao, J.; Xu, T.; Deng, J.; Yang, F.; Duchesne, P. N.; Zhang, P.; Zhou, J.; Sun, L.; Li, J.; Pan, X.; Bao, X. A single iron site confined in a graphene matrix for the catalytic oxidation of benzene at room temperature. Sci. Adv. 2015, 1, No. e1500462.
- (56) Yang, H. B.; Hung, S.-F.; Liu, S.; Yuan, K.; Miao, S.; Zhang, L.; Huang, X.; Wang, H.-Y.; Cai, W.; Chen, R.; Gao, J.; Yang, X.; Chen, W.; Huang, Y.; Chen, H. M.; Li, C. M.; Zhang, T.; Liu, B. Atomically dispersed Ni (I) as the active site for electrochemical CO₂ reduction. Nat. Energy 2018, 3, 140-147.
- (57) Calace, N.; Nardi, E.; Petronio, B. M.; Pietroletti, M. Adsorption of phenols by papermill sludges. Environ. Pollut. 2002, 118, 315-319.
- (58) Costentin, C.; Louault, C.; Robert, M.; Savéant, J.-M. The electrochemical approach to concerted proton—electron transfers in the oxidation of phenols in water. Proc. Natl. Acad. Sci. U.S.A. 2009, 106, 18143-18148.
- (59) Costentin, C.; Louault, C.; Robert, M. Evidence for concerted proton-electron transfer in the electrochemical oxidation of phenols with water as proton acceptor. tri-tert-butylphenol. J. Am. Chem. Soc. **2008**, *130*, 15817–15819.
- (60) Mao, R.; Li, N.; Lan, H.; Zhao, X.; Liu, H.; Qu, J.; Sun, M. Dechlorination of trichloroacetic acid using a noble metal-free graphene-Cu foam electrode via direct cathodic reduction and atomic H. Environ. Sci. Technol. 2016, 50, 3829-3837.
- (61) Li, J.; Wang, H.; Qi, Z.; Ma, C.; Zhang, Z.; Zhao, B.; Wang, L.; Zhang, H.; Chong, Y.; Chen, X.; Cheng, X.; Dionysiou, D. D. Kinetics and mechanisms of electrocatalytic hydrodechlorination of diclofenac on Pd-Ni/PPy-rGO/Ni electrodes. Appl. Catal., B 2020, 268, 118696.

- (62) Lou, Z.; Wang, Z.; Zhou, J.; Zhou, C.; Xu, J.; Xu, X. Pd/TiC/Ti electrode with enhanced atomic H* generation, atomic H* adsorption and 2, 4-DCBA adsorption for facilitating electrocatalytic hydrodechlorination. *Environ. Sci.: Nano* **2020**, *7*, 1566–1581.
- (63) Fan, L.; Liu, P. F.; Yan, X.; Gu, L.; Yang, Z. Z.; Yang, H. G.; Qiu, S.; Yao, X. Atomically isolated nickel species anchored on graphitized carbon for efficient hydrogen evolution electrocatalysis. *Nat. Commun.* **2016**, *7*, 10667.
- (64) Peng, Y.; Cui, M.; Zhang, Z.; Shu, S.; Shi, X.; Brosnahan, J. T.; Liu, C.; Zhang, Y.; Godbold, P.; Zhang, X.; Dong, F.; Jiang, G.; Zhang, S. Bimetallic composition-promoted electrocatalytic hydrodechlorination reaction on silver—palladium alloy nanoparticles. *ACS Catal.* **2019**, *9*, 10803—10811.
- (65) Gravil, P. A.; Toulhoat, H. Hydrogen, sulphur and chlorine coadsorption on Pd (111): a theoretical study of poisoning and promotion. *Surf. Sci.* **1999**, *430*, 176–191.
- (66) Hensley, A. J. R.; Wang, Y.; McEwen, J.-S. Adsorption of phenol on Fe (110) and Pd (111) from first principles. *Surf. Sci.* **2014**, 630, 244–253.
- (67) López, E.; Ordóñez, S.; Díez, F. V. Deactivation of a Pd/Al₂O₃ catalyst used in hydrodechlorination reactions: Influence of the nature of organochlorinated compound and hydrogen chloride. *Appl. Catal., B* **2006**, *62*, 57–65.
- (68) Roth, D.; Gélin, P.; Primet, M.; Tena, E. Catalytic behaviour of Cl-free and Cl-containing Pd/Al2O3 catalysts in the total oxidation of methane at low temperature. *Appl. Catal.*, A **2000**, 203, 37–45.
- (69) Miranda, B.; Díaz, E.; Ordóñez, S.; Vega, A.; Díez, F. V. Performance of alumina-supported noble metal catalysts for the combustion of trichloroethene at dry and wet conditions. *Appl. Catal., B* **2006**, *64*, 262–271.
- (70) Arenz, M.; Stamenkovic, V.; Schmidt, T. J.; Wandelt, K.; Ross, P. N.; Markovic, N. M. The effect of specific chloride adsorption on the electrochemical behavior of ultrathin Pd films deposited on Pt(111) in acid solution. *Surf. Sci.* **2003**, *523*, 199–209.
- (71) Liu, J.; Lucci, F. R.; Yang, M.; Lee, S.; Marcinkowski, M. D.; Therrien, A. J.; Williams, C. T.; Sykes, E. C. H.; Flytzani-Stephanopoulos, M. Tackling CO poisoning with single-atom alloy catalysts. *J. Am. Chem. Soc.* **2016**, *138*, 6396–6399.
- (72) Lu, Y.; Wang, J.; Yu, L.; Kovarik, L.; Zhang, X.; Hoffman, A. S.; Gallo, A.; Bare, S. R.; Sokaras, D.; Kroll, T.; Dagle, V.; Xin, H.; Karim, A. M. Identification of the active complex for CO oxidation over single-atom Ir-on-MgAl₂O₄ catalysts. *Nat. Catal.* **2018**, *2*, 149–156.
- (73) Pieta, I. S.; Kadam, R. G.; Pieta, P.; Mrdenovic, D.; Nowakowski, R.; Bakandritsos, A.; Tomanec, O.; Petr, M.; Otyepka, M.; Kostecki, R.; Khan, M. A. M.; Zboril, R.; Gawande, M. B. The hallmarks of copper single atom catalysts in direct alcohol fuel cells and electrochemical CO₂ fixation. *Adv. Mater. Interfaces* **2021**, *8*, 2001822.
- (74) Liu, H.; Han, J.; Yuan, J.; Liu, C.; Wang, D.; Liu, T.; Liu, M.; Luo, J.; Wang, A.; Crittenden, J. C. Deep dehalogenation of florfenicol using crystalline CoP nanosheet arrays on a Ti plate via direct cathodic reduction and atomic H. *Environ. Sci. Technol.* **2019**, *53*, 11932–11940.
- (75) Lymar, S. V.; Schwarz, H. A. Hydrogen atom reactivity toward aqueous tert-butyl alcohol. *J. Phys. Chem. A* **2012**, *116*, 1383–1389.
- (76) Hardison, D. R.; Cooper, W. J.; Mezyk, S. P.; Bartels, D. M. The free radical chemistry of tert-butyl formate: rate constants for hydroxyl radical, hydrated electron and hydrogen atom reaction in aqueous solution. *Radiat. Phys. Chem.* **2002**, *65*, 309–315.
- (77) Min, Y.; Zhou, X.; Chen, J.-J.; Chen, W.; Zhou, F.; Wang, Z.; Yang, J.; Xiong, C.; Wang, Y.; Li, F.; Yu, H.-Q.; Wu, Y. Integrating single-cobalt-site and electric field of boron nitride in dechlorination electrocatalysts by bioinspired design. *Nat. Commun.* **2021**, *12*, 303.